Research article

A computational study on the molecular mechanisms of panduratin A as a potential inhibitor on SARS-CoV-2 protein targets

Patamalai Boonserm [a], Pongsak Khunrae [a], Thana Sutthibutpong [b,c,*]

[a] *Department of Microbiology, Faculty of Science, King Mongkut's University of Technology Thonburi, Bangkok, Thailand*
[b] *Department of Physics, Faculty of Science, King Mongkut's University of Technology Thonburi, Bangkok, Thailand*
[c] *Center of Excellence in Theoretical and Computational Science (TACS-CoE), Faculty of Science, King Mongkut's University of Technology Thonburi, Bangkok, Thailand*

A R T I C L E   I N F O

A B S T R A C T

Panduratin A from *Boesebergia rotunda* was recently reported as a potent anti-SARS-CoV-2 compound. However, the molecular mechanisms underlying the inhibition by Panduratin A and its target remained unclear. Molecular docking calculations were performed between panduratin A and five important proteins, i.e., main protease (Mpro), papain-like protease (PLpro), receptor binding domain (RBD) of spike proteins, RNA-dependent-RNA-polymerase (RdRp), and 2'-O-methyltransferase (MTase). The estimated binding free energy and the interaction networks extracted from the best docking mode for each complex suggested that MTase was the most probable target for panduratin A inhibition. To further validate the ability of panduratin A to inhibit MTase, molecular dynamics (MD) simulations and binding free energy calculations were performed for panduratin A-MTase complex, in comparison with another MTase complex with sinefungin as a positive control. Chemical features of panduratin A and sinefungin were compared for their contribution in MTase binding. It was found that both molecules could bind to the S-Adenosyl methionine (SAM) binding pocket and prevent the SAM entrance co-substrate, which could eventually halt the function of MTase. Despite a slightly weaker binding free energy, the equilibrated positional binding of panduratin A was found at a closer distance to the active sites. Therefore, this study proposed MTase as a possible target of panduratin A, along with the mechanisms of inhibition, prompting another future *in vitro* study as a verification.

1. Introduction

The new coronavirus disease (COVID-19) caused by the severe acute respiratory syndrome coronavirus 2 (SARS-CoV-2) has dramatically spread worldwide. As a result, the World Health Organization (WHO) raised the severity level of COVID-19 to a pandemic disease [1]. SARS-CoV-2 is an enveloped, positive-sense single-stranded RNA virus [2]. The viral RNA genome contains approximately 30,000 nucleotide bases and 11 open reading frames (ORF). The replicase polyprotein consisted of six functional ORFs: replicase (ORF1a/ORF1b), spike (S), envelope (E), membrane (M), and nucleocapsid (N) [3,4]. Ribosomal frameshifting-dependent translation

---

of the replicase genes ORF1a and ORF1b forms two polyproteins, pp1a and pp1ab, which are cleaved into 16 nonstructural proteins (nsp1-16) by the viral papain-like protease (PLpro, nsp3) and main protease or 3C-like protease (Mpro or 3CLpro, nsp5) [5].

The SARS-CoV-2 infected the host cell with the glycosylated spikes (S) protein, which extended from the coronavirus particles' envelope. The spike protein is strongly related to human pathogens due to its ability to bind with an Angiotensin-converting enzymes-2 (ACE-2) on a human cell surface, which leads to the fusion of viral and cell membranes [6,7]. Furthermore, other crucial viral proteins of the SARS-CoV-2 for the viral life cycle were the RNA dependent RNA polymerase (RdRp) (nsp12), which initiates viral replication and transcription [8], and RNA methyltransferases (Mtase or nsp16), which produce new full-length nucleocapsid-encapsidated viral RNA genome in the endoplasmic reticulum (ER) involved in several biological processes such as viral signal transduction, nucleic acid processing, chromatin remodeling, metabolism, detoxification, and mRNA capping [9,10]. The receptor binding domain (RBD) of spike proteins, RdRp, MTase, and PLpro and Mpro, were shown to play important roles in the SARS-CoV-2 infection and life cycles and thus became the targets for drug development.

On November 24, 2021, WHO reported the new variant of concern B.1.1.529, known as omicron. Another dramatic spread caused by omicron was in concurrence with the 11 mutations in the RBD of spike proteins, binding to the ACE2 and other human receptors during viral infection. Recent studies showed that a mutation replacing a glutamine with an arginine at position 498 (Q498R) resulted in an increase of ACE2 binding affinity by more than 1000-fold when combined with the N501Y mutation [11,12]. Furthermore, other mutations also caused the omicron variant to evade vaccinations and immune systems [13]. Fortunately, the high binding affinity on human receptors should also hamper the ability of omicron to penetrate deep into lung tissues [14]. Thus, the symptoms of omicron became 91% less fatal than the delta variant, and COVID-19 became more likely a wider spreading but less severe endemic.

Therefore, herbal medicine could be another good choice for boosting immunity against the COVID-19 variants due to lower prices and fewer side effects. Apart from the experimental studies on testing the bioactivities of the herbal extract on COVID-19, computational approaches were used to gain insight into the inhibition mechanisms at the molecular level. The examples included a study by Almeida-Neto et al. that discovered the molecular mechanisms of 4′-acetamidechalcones on inhibiting critical enzymes during the post-translation process of SARS-CoV-2 virus [15]. Another study by Nouadi et al. employed the molecular docking approach to predict the potential treatment for COVID-19 by compounds from medicinal plants in Morocco, including taxol, rutin genkwanine, and luteolin-glucoside [16]. Considering the structure of the repurposed nucleoside analogs, including remdesivir, the RNA-dependent-RNA-polymerase (RdRp) could also be targeted and also had proven effective in clinical trials. Gao et al. [18,19] used a comparative analysis model of the remdesivir-RdRp complex to design new antiviral therapeutics that target viral RdRp. Similarly, Singh et al. [20] used molecular docking to compare the binding affinity and interaction networks of selected tea bioactive compounds with the standard molecule sinefungin to demonstrate their ability to inhibit the non-structural protein 16 (nsp16) of SARS-CoV-2.

This study focused on another herbal medicine of great interest in Thailand, inspired by a recent work of Kanjanasirirat et al. (2020) [21], which reported a potent anti-SARS-CoV-2 activity of panduratin A from *Boesebergia rotunda*. The exact target protein inhibited by panduratin A and the molecular mechanisms of inhibition remained unidentified. Therefore, inhibition of panduratin A will be theoretically investigated at the molecular level using molecular docking and atomistic molecular dynamics (MD) simulations to analyze the intermolecular interactions between panduratin A and five candidates for protein target: (i) RBD of a spike protein, (ii) Mpro, (iii) PLpro, (iv) RdRP, and (v) MTase, identified earlier as essential parts for COVID-19 infection and viral life cycle. A total understanding of inhibition mechanisms at the molecular level should provide insight into the development of panduratin A as an immunity booster or to reduce the symptom of COVID-19 infection.

2. Material and methods

2.1. Compounds and protein target models preparations

The three-dimensional structure of a panduratin A molecule for molecular docking calculation was obtained from the PubChem database. Then, the molecular structures were optimized by the MMFF94 force field implemented within the Avogadro software. Crystal structures of some important protein targets for panduratin A were retrieved from the Protein Data Bank (https://www.rcsb.org/): the SARS-CoV-2 spike receptor-binding domain bound with ACE2 (PDB ID: 6M0J), SARS-CoV-2 main protease (Mpro) (PDB ID: 6LU7), the enzyme SARS-CoV-2 papain-like protease (PLpro) (PDB ID: 6WX4), RNA-dependent RNA polymerase (RdRP) (PDB ID: 4WTG), 2′-O-methyltransferase (nsp16-nsp10 heterodimers)) (PDB ID: 6WKQ). Then, the protein structures were prepared for molecular docking calculations by removing all water and non-protein residues.

2.2. Molecular docking

Molecular docking was employed as a tool for the first-step prediction of compound binding postures to the target proteins of SARS-CoV-2. Firstly, three-dimensional coordinates of compounds and target proteins were imported to AutoDockTools [22] for docking setting up; Gasteiger partial charges were assigned to all-atom, and non-polar hydrogen atoms were merged with carbon atoms using the united atom representation to reduce the degrees of freedom. The interaction interface residues were then defined within a three-dimensional grid that limit the atomic positions of the docked compounds. The search space was created for each docking calculation by setting the coordinates of the box center at a sidechain atom of a catalytic residue and setting the search space dimension to cover the binding pocket. The search spaces for the five target proteins were set to (1) dimension 26 Å × 40 Å × 18 Å, centered at −36.686, 30.239, −3.055 (XYZ coordinates), for the spike protein (6M0J), (2) dimension 26 Å × 24 Å × 32 Å, centered at −18.503, 16.174, 64.314 (XYZ coordinates) for Mpro (6LU7), (3) dimension 26 Å × 16 Å × 34 Å centered at 9.087, −19.201, −39.27 (XYZ

coordinates) for PLpro (6WX4), (4) dimension 40 Å × 40 Å × 40 Å centered at 185.542, 170.172, 159.465 (XYZ coordinates) for RdRp (7L1F), and (5) dimension 36 Å × 28 Å × 40 Å centered at 91.817, 10.607, −0.713 (XYZ coordinates) for nsp16 interface (6WKQ). Then, molecular docking with the Lamarckian genetic algorithm and knowledge-based scoring function was performed using the AutoDock Vina software by a modified protocol from Muhammad et al. (2020) [23]. The best 20 conformers of the compound-target protein complex, ranked by the estimated binding free energy score, will be generated during the docking process and were visualized by the AutoDockTools program. Finally, the protein target with the best binding energy score among all five docking calculations was chosen as the starting structure for an explicitly solvated molecular dynamics simulation.

The binding models were examined using PyMOL Stereo 3D Quad-buffer (licensed version 2.5.1, Schrödinger Inc, USA) and Discovery Studio 2021 (free version, BIOVIA Inc, China) was used to predict the interaction network between the target proteins and ligands.

2.3. Molecular dynamics (MD) simulations and analysis

Explicitly solvated MD simulations for the protein-ligand complexes of 1) the selected protein target and panduratinA, and 2) the selected protein target and a known drug molecule to that protein target, were carried out with the GROMOS54A7 force field [24] in GROMACS package version 5.1.2 [25]. The starting structure of each compound-protein complex was taken from the molecular docking results by the AutoDock Vina. The Force field for each ligand was generated from the Automated Topology Builder (ATB) webserver [26] with the GROMOS54A7 force field. The simple point-charge (SPC) solvent model with 1 nm buffer distance and Na^+ or Cl^- counterions that neutralized the system was then used to solvate the structure of NSP16 complexes (Table 1). Each simulation was subjected to energy minimization using the steepest descent technique, and a 1-ns equilibration run was performed for each simulation, in which each structure was gradually heated from 100 K to 300 K. Finally, each equilibrated structure was put into a 50 ns productive MD run in the NPT ensemble at 300 K and 1 atm pressure. The velocity-rescale algorithm was used to control the temperature, while the Berendsen barostat was used to control the pressure. The Particle-Mesh-Ewald (PME) approach was utilized to establish the periodic boundary condition for the explicitly solvated systems and the 1-nm cutoff distance was used for the short-range interaction. Finally, the P-LINC algorithm applied geometrical constraints on the covalent bonds associated with hydrogen atoms so that a 2-fs timestep size was allowed. After all simulations finished, water molecules were removed from the trajectory along with the translational and rotational motions. Only internal motions of the protein-ligand complex were analyzed. Then root mean square deviation (RMSD) was calculated from each simulation to track the overall conformational changes of the protein and the ligand. The per-residue root mean square fluctuations (RMSF) were calculated to assess the local flexibility and rigidity induced by ligand binding. For each simulation, minimum distance between the catalytic site and the inhibitor was also presented for each timestep by considering the distance between all possible atom pairs from two groups: (i) catalytic residues and (ii) inhibiting compound. The visual molecular dynamics (VMD) software was used to visualize the molecular trajectories [27].

Table 1
Docking score of the Panduratin A against the SARS-CoV-2 target proteins using AutoDock Vina.

SARS-CoV-2 target proteins	Vina scores (kcal/mol)
Receptor-binding domain (RBD) of spike glycoprotein	-6.5
	-6.5
	-6.3
	-6.0
	-5.9
Main protease (Mpro)	-6.6
	-6.5
	-6.2
	-6.1
	-6.0
Papain-like protease (PLpro)	-4.9
	-4.8
	-4.8
	-4.6
	-4.6
RNA-dependent RNA polymerase (RdRp)	-6.9
	-6.7
	-6.7
	-6.7
	-6.7
2′-O-methyltransferase (MTase)	-7.2
	-7.1
	-7.1
	-7.1
	-7.0

2.4. MM/PBSA calculations of binding free energy

The binding free energy was calculated by using an MM/PBSA from the g_mmpbsa package. Binding free energy of the protein-ligand complex could be formally calculated as follows:

$$\Delta G_{bind} = \Delta G_{complex} - \Delta G_{protein} - \Delta G_{ligand} \qquad (1)$$

$$\Delta G_{bind} = \Delta E_{MM} + \Delta G_{solv} \qquad (2)$$

$$\Delta E_{MM} = \Delta E_{elec} + \Delta E_{vdw} \qquad (3)$$

$$\Delta G_{solv} = \Delta G_{polar} + \Delta G_{nonp} \qquad (4)$$

where, ΔG_{bind}, $\Delta G_{complex}$, $\Delta G_{protein}$, ΔG_{ligand} in equation (1) are the total binding free energy, the free energy of the binding complex, protein, and ligand, respectively. Within an implicit solvent environment described in the term ΔG_{solv}, components within the total binding free energy ΔG_{bind} in equation (2) also included the contribution from molecular mechanics (ΔE_{MM}) term. ΔE_{MM} is the potential energy in vacuum as defined by the molecular mechanics model, which exhibits the total change in non-covalent molecular mechanics energy in the gas phase using the GROMOS54A7 force field. According to equation (3), the contributions from molecular mechanics energy included the van der Waals term (ΔE_{vdw}) for the non-polar and hydrophobic contacts and the Coulombic term (ΔE_{elec}) for polar contacts and hydrogen bonding. Finally, ΔG_{solv} is the free energy of solvation from the Poisson-Boltzmann surface area (PBSA) approach. From equation (4), ΔG_{solv} is contributed by a polar (ΔG_{polar}) and a non-polar (ΔG_{nonp}) terms from the calculations of PBSA energy from polar solvation and the calculations of non-polar solvation energy from the solvent accessible surface area (SASA). Protein dielectric constant was set to 4, solvent dielectric constant to 80, and ion concentration to 0.006 M, corresponding to 2 Cl^- counterion. Next, the non-polar solvation energy was calculated using the solvent-accessible surface area (SASA) model. Non-polar solvation energy due to surface tension increases linearly with surface area in the SASA model. Therefore, the surface tension of the solvent was set to 0.0226778 kJ/(mol $\mathring{A}^2$) in our calculation, and the SASA energy constant was set to 3.84982 kJ/mol. For snapshots taken every 0.1 ns from the last NSP16 complex MD trajectories, MM/PBSA calculations were performed, generating time averages of total binding free energy and contributions from MM energy, polar and non-polar solvation. Per residue energy decomposition was also performed to determine the contribution of each amino acid residue to total binding free energy.

3. Results and discussions

3.1. Binding interactions of panduratin A with target proteins from molecular docking calculations

Panduratin A from *Boesenbergia rotunda* was recently reported as a potent anti-SARS-CoV-2 compound. Molecular structure of a panduratin A molecule (see Fig. 1) consisted of three ringed structures: (i) phenyl ring (Ring I), (ii) methyl cyclohexene (Ring II), and (iii) methoxylated benzenediol (Ring III). The Ring II was connected to a 2-methyl-2-butane tail and a carbonyl group linked to Ring III. The exact molecular mechanisms for how panduratin A was active against SARS-CoV-2 remained unknown. Therefore, molecular docking calculations were performed to search for the most probable binding postures of panduratin A on five important target proteins of SARS-CoV-2. Table 1 displayed the estimated binding affinity of the five best binding modes from each complex calculated from the combined knowledge-based and empirical scoring function of Autodock Vina. After that, interaction network diagrams were obtained from the best binding mode of all protein-ligand complexes (Fig. 2) and contribution of each panduratin A functional groups was summarized in Table 2.

Fig. 2a showed the best panduratin A docked configuration on the SARS-CoV-2 spike receptor-binding domain (RBD) with a binding energy score of −6.5 kcal/mol. A hydrogen bond was formed between the Ser494 residue of RBD and a hydroxyl group of Ring III, while another was formed between the backbone of Gly496 and the linking carbonyl group. Moreover, six hydrophobic contacts
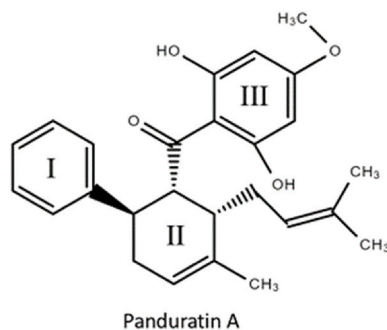

Fig. 1. Schematic representation of a Panduratin A molecule displaying all functional groups. Ringed structures labelled as Ring I, Ring II, and Ring III were used as references for Tables 2 and 4.
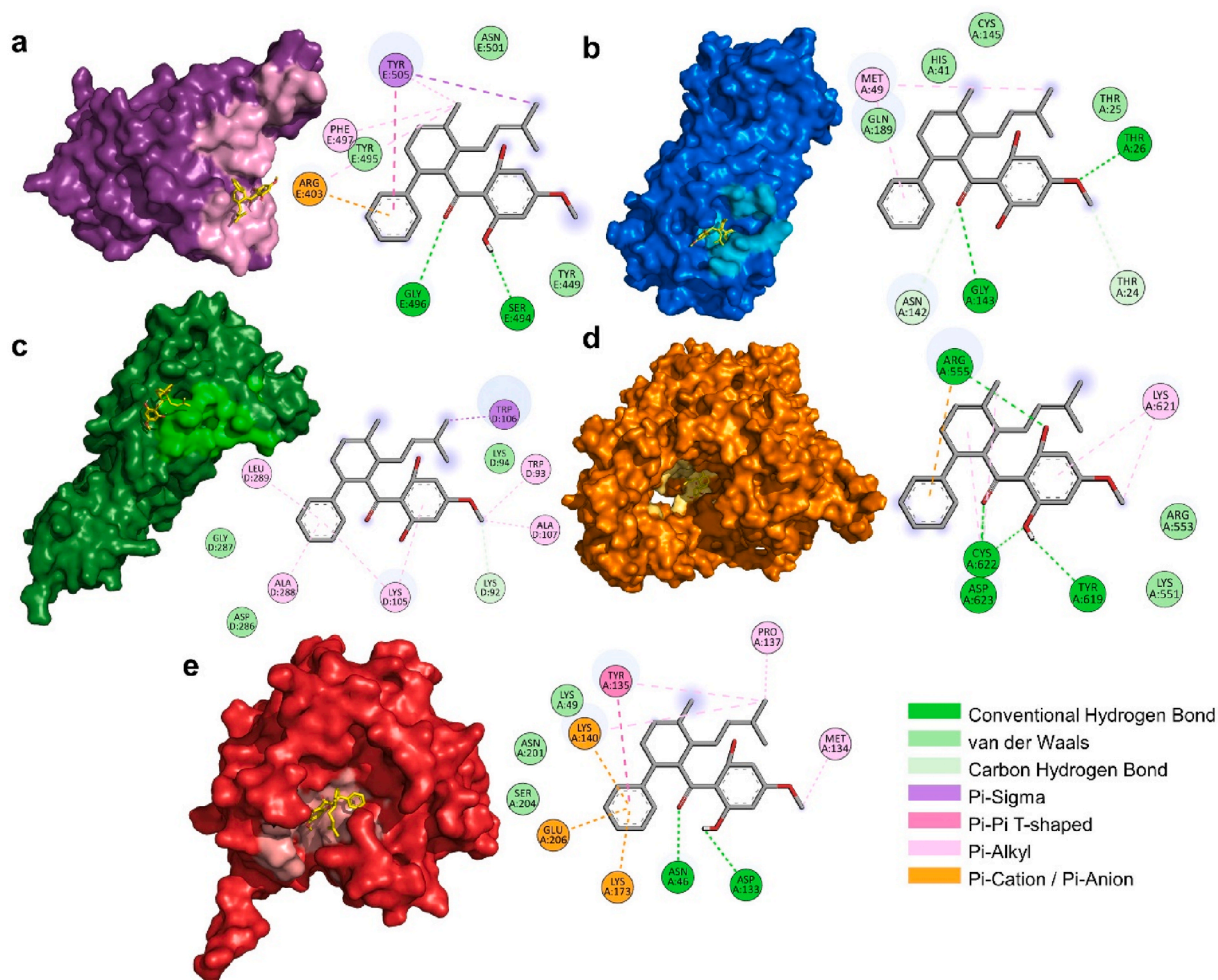
Fig. 2. Molecular interactions between Panduratin A and the SARS-CoV-2 target proteins were generated using PyMOL: (top) (**a**) Receptor-binding domain (RBD) of spike glycoprotein (magenta), (**b**) Main protease (Mpro) (blue), (**c**) Papain-like protease (PLpro) (green), (**d**) RNA-dependent RNA polymerase (RdRp) (light orange) and (**e**) 2′-O-methyltransferase (nsp16) (red). The 2D images were generated using the Discover studio 2021 Client. (For interpretation of the references to colour in this figure legend, the reader is referred to the Web version of this article.)

found at the Arg403, Tyr495, Phe497, and Tyr505 residues of spike receptor-binding domain were contributed by the Ring I, Ring II, and the 2-methyl-2-butane tail. The best-docked configuration of panduratin A on the Mpro protein in Fig. 2b was with a binding energy score of −6.6 kcal/mol. Thr24 and Thr26 residues of Mpro formed a carbon-hydrogen bond and a hydrogen bond with Ring III, respectively. Similarly, the linking carbonyl group formed a carbon-hydrogen bond with Asn142, and a hydrogen bond with Gly143. The Met49 residue formed hydrophobic contacts both with the Ring I and the 2-methyl-2-butane tail and brought the ligand into proximity with the catalytic site of residues Cys145 and His41 [28,29]. Hydrophobic interactions contributed by Met49, Asn142, Gly143, and the catalytic residue Cys145 were also found in the interaction network of an N3 inhibitor docked within the Mpro binding cleft with additional hydrophobic contacts (Supplementary Fig. 1).

The best-docked configuration of panduratin A on a PLpro is shown in Fig. 2c. The Ring III formed a weak carbon-hydrogen bond with Lys92 residue of PLpro and formed weak Pi-Alkyl interactions with the Trp93, Lys105, Ala107, Ala288, and Leu289. Despite the Trp106 residue forming a Pi-sigma interaction with the 2-methyl-2-butane tail, the predicted binding energy score between a panduratin A on a PLpro was −4.9 kcal/mol, relatively weaker than the other protein targets. The interaction network between a PLpro and remdesivir also displayed the contribution from Ala288 and Leu289, but with significantly larger subnetwork of pi interactions with Trp106 (Supplementary Fig. 1). The panduratin A was also docked into the catalytic site of an RdRp enzyme of SARS-CoV-2 (Fig. 2d). The Arg555, Tyr619, and Cys622 residues of RdRp formed hydrogen bonds with the Ring III, while another hydrogen bond was formed between the Asp623 residue and the linking carbonyl group. Moreover, Arg555 formed another strong Pi-cation interaction with the Ring I, along with the four weak Pi-Alkyl interactions at the Lys621 and Cys622 residue pair. The highest amount of hydrogen bonds formed between panduratin A and RdRp relative to other ligands brought the lowest binding energy to reach −6.9 kcal/mol. The best docked configuration of remdesivir on the RdRp protein also displayed interactions contributed by

Table 2
Types of hydrogen bonds and hydrophobic contacts between functional groups of panduratin A and the amino acids of protein targets.

Functional groups	S-RBD	Mpro	PLpro	RdRp	MTase
aromatic (Ring I)	Arg403	Met49	Lys105	Arg555	Tyr135
	Tyr505		Ala288		Lys140
			Leu289		Lys173
					Glu206
methyl cyclohexene (Ring II)	Arg403			Cys622	
	Phe497				
	Tyr505				
2-methyl-2-butene	Tyr505	Met49	Trp106		Tyr135
					Pro137
					Lys140
carbonyl	Gly496	Asn142		Cys622	Asn46
		Gly143		Asp623	
aromatic (Ring III)			Lys105	Lys621	
methoxyl (Ring III)		Thr24	Lys92	Lys621	Met134
		Thr26	Trp93		
			Ala107		
hydroxyl (Ring III)				Arg555	
	Ser494			Tyr619	Asp133
				Cys622	

* Conventional hydrogen bond (green), carbon hydrogen bond (light green), Pi-sigma (purple), Pi-Pi T-shaped (pink), Pi-alkyl (light pink), Pi-cation/Pi-anion (orange)

Arg555, Tyr619, Cys622, and Asp623, but with a significantly larger number of hydrogen bonds (Supplementary Fig. 1).

Finally, the best-docked configuration of panduratin A on a 2′-O-methyltransferase (MTase) shown in Fig. 2e formed two hydrogen bonds between the Asn46 residue and the linking carbonyl group, and between the Asp133 residue and the hydroxyl group of Ring III. In addition, the ligand also formed Pi-alkyl interactions with Met134, Tyr135, and Pro137, as well as the Pi-Pi T-shape interaction between Tyr135 and the Ring I. Moreover, three Pi-cation and Pi-anion interactions involving residues Lys140, Lys173, and Glu206 and Ring I, along with two more hydrogen bonds, contributed to the strongest ligand binding on the target protein with the binding energy score of −7.2 kcal/mol. The best docked configuration of sinefungin on the MTase also displayed interactions contributed by residues 133–137, but not the catalytic residues Lys49 and Glu206 (Supplementary Fig. 1).

The interaction networks between each functional group of panduratin A and amino acids of the five proposed target proteins were summarized in Table 2. It was found that the binding pocket residues of RdRp and MTase occupied almost all the functional groups of panduratin A. Moreover, MTase had the highest number of amino acid residues involving the interactions, suggesting the highest coverage of panduratin A on the binding pocket, and was in concurrence with the strongest binding energy predicted by molecular docking calculations. Therefore, MTase could be a possible target of panduratin A and became the main focus of further simulations and analysis through molecular dynamics simulations.

3.2. Molecular dynamics simulations and analysis on the binding mechanisms of panduratin A compared with a known inhibitor

Molecular docking calculations and interaction analysis between panduratin A and five important protein targets for the SARS-CoV-2 life cycle showed that binding of panduratin A on the 2′-O-methyltransferase (MTase) protein, was with the highest affinity, in concurrence with the highest degree of the protein-ligand interaction network. Therefore, molecular docking results suggested that MTase became the most probable target for panduratin A. The nsp16 domain of MTase (see Fig. 3) contained a large beta-sheet surrounded by alpha helices at the core of the domain. Furthermore, the panduratin A from our docking calculation was shown to partly interact with the S-Adenosyl methionine (SAM) binding pocket, near another pocket for RNA substrate binding [28]. SAM was the co-substrate for the methyl group transfer as it donated a methyl group from the sidechain for the RNA substrate. It was an interesting target for inhibitors, e.g., sinefungin, a natural nucleoside from *Streptomyces* species previously known for antiviral and antifungal activities.

To further confirm the prediction from molecular docking results, the positional binding of panduratin A on MTase was compared to that of sinefungin, an inhibitor for MTase. In this section, molecular dynamics (MD) simulations, and conformational analysis and binding free energy calculations, were performed to investigate the binding stability and molecular interactions of panduratin A and sinefungin binding on the MTase protein domain. Temperature and pressure regulation in each simulation brought the environment of the explicitly solvated simulation box closer to the physiological conditions.
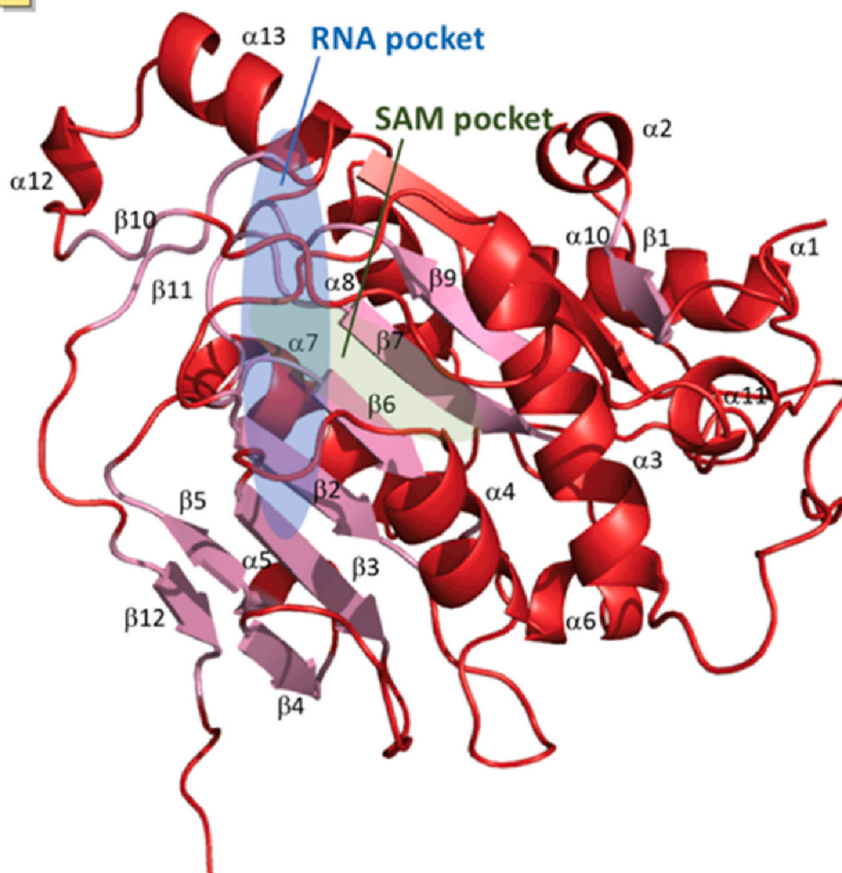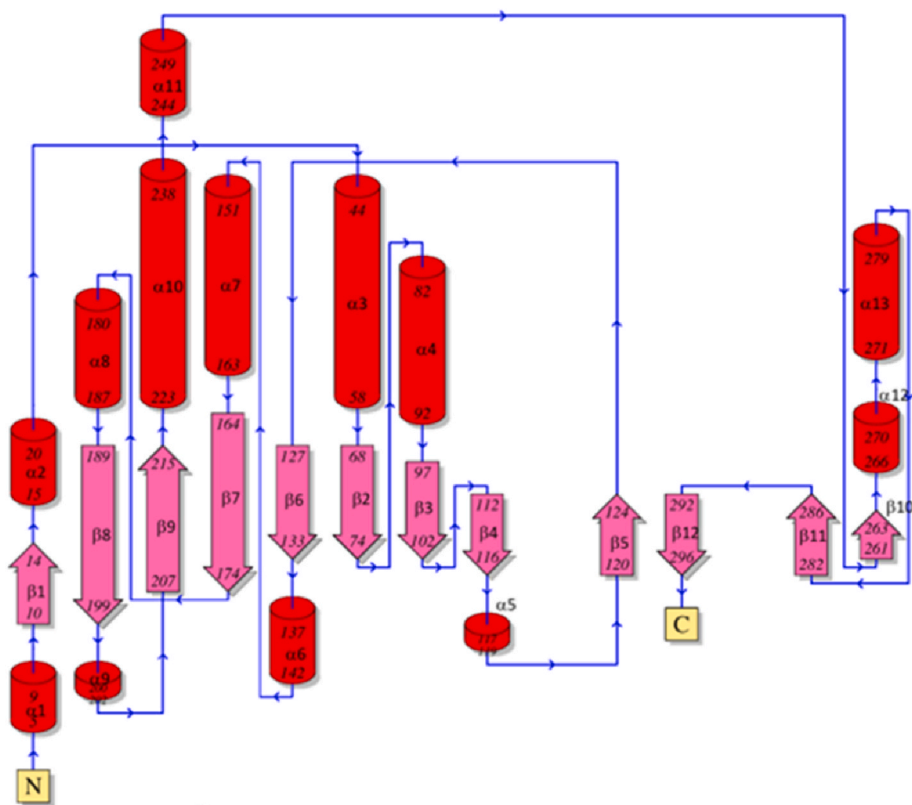
(caption on next page)

Fig. 3. (top) topological diagram of all secondary structures within the nsp16 domain of 2′-O-methyltransferase (MTase) from SARS-CoV-2. Amino acid residue numbers are labelled along with alpha helices (cylinders) and beta sheets (arrows), (bottom) 3D conformation of the nsp16 domain with all alpha helices and beta sheets labelled. RNA and SAM pocket were also highlghted.

After each of the 50-ns simulations finished, root mean square deviation (RMSD) was calculated along each simulated trajectory to investigate the stability of ligand binding under the condition near the physiological environment. The RMSD of the protein structures from both simulated complexes rapidly increased to 0.25 nm during the first 2 ns and then converged to around 0.3 ns after 10 ns. The sharp increase of the RMSD at the beginning signified the global changes in the protein structures from both simulations when the environment was switched from the crystalized state to the solvated state. The convergence of both RMSD plots suggested that both simulations reached their equilibriums and remained equilibrated from 10 ns to 50 ns (Fig. 4a). Only an insignificant difference was observed between the RMSD of both simulations, indicating that the stability of the MTase protein under a solvated environment was unaffected by the different ligands. Then, the local flexibility of the protein in both simulations was assessed through the per-residue root mean square fluctuation (RMSF). From the RMSF profiles in Fig. 4b, peaks with high RMSF reflected the high flexibility of loop regions linking between alpha helices and beta sheets, at which RMSF values were lower. Interestingly, RMSF peaks of the two simulated complexes were found to be the difference at the ligand-bound residues. RMSF around the β3/β4 loop and β4/α5 loop regions (residues 100–114) of the MTase-panduratin A complex were with the higher RMSF, suggesting that both β3/β4 and β4/α5 regions of MTase-panduratin A complex were relatively unstable. However, another binding site within the long α6/α7 loop (residues 137–147) of the MTase-panduratin A complex was lower RMSF and higher stability than the MTase-sinefungin complex. Therefore, the conformational analysis by RMSD and RMSF calculations from the trajectories of both complexes containing a panduratin A and a sinefungin, as a known inhibitor, suggested that these two ligands caused an insignificant difference in global conformational changes of the MTase protein, but local flexibility of binding sites were varied by binding of different ligands. The ligand RMSD in Fig. 4c for both simulations also became converged to around 0.3–0.5 nm after 10 ns, indicated that the positional binding of both panduratin A and sinefungin was slightly shifted. The RMSD profiles calculated from MD simulations during 10–50 ns were in agreement with RMSD calculated from the first five binding modes relative to the best binding modes (See Supplementary Table 1).

The molecular mechanics and Poisson-Boltzmann surface approximation (MM/PBSA) calculations further elucidated the binding mechanism and strength. The molecular mechanics (MM) terms accounted for the potential energy from electrostatics and van der Waals terms, mainly contributed by hydrogen bonds and hydrophobic contacts, respectively. The Poisson-Boltzmann surface approximation (PBSA) term accounted for the energy from solvation or the surface contact between the complexes and the solvent. Binding free energy was obtained by the difference between the MM/PBSA energy of a protein-ligand complex and the total MM/PBSA
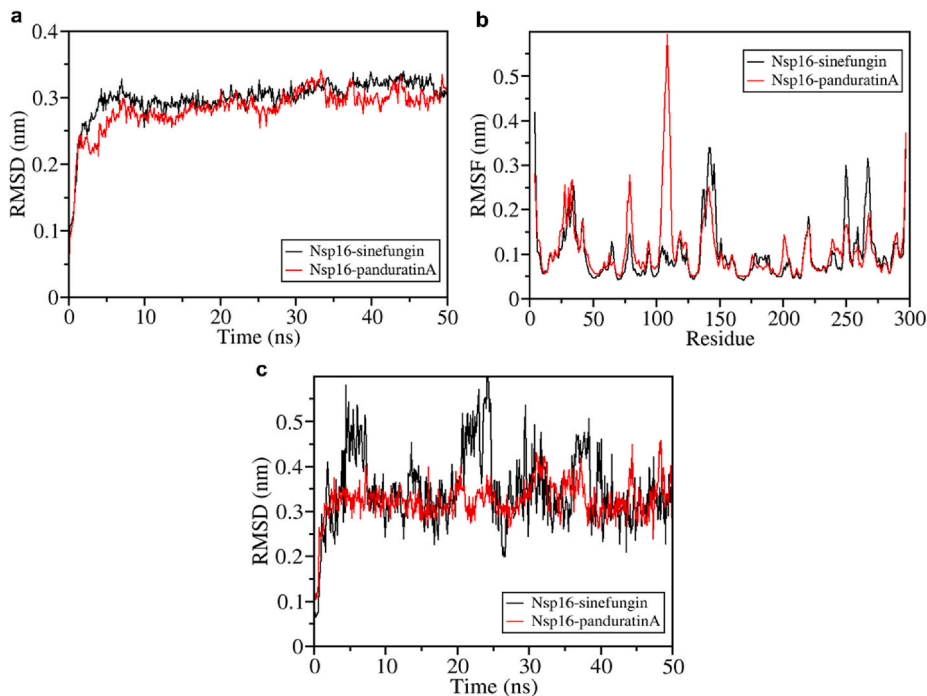

Fig. 4. RMSD and RMSF profile for MTase-sinefungin (black line) and MTase-panduratin A (red line): (**a**) The root mean square deviation (RMSD) of the backbone atoms from the equilibrated conformation (0–50 ns), (**b**) Root mean square fluctuation (RMSF) values of atomic positions computed for the backbone atom are shown as a function of residue number, and (**c**) The root mean square deviation (RMSD) of the ligand atoms from the equilibrated conformation (0–50 ns). (For interpretation of the references to colour in this figure legend, the reader is referred to the Web version of this article.)

Table 3
Binding free energy factors for the protein-ligand complexes calculated by MM-PBSA analysis.

Complex	$\Delta E_{Binding}$ (kJ/mol)	$\Delta E_{Vander\ Waal}$ (kJ/mol)	$\Delta E_{Electrostatic}$ (kJ/mol)	$\Delta E_{Polar\ solvation}$ (kJ/mol)	$\Delta E_{non\text{-}Polar}$ (kJ/mol)
Panduratin A-MTase	-128 ± 21	-174 ± 15	-13 ± 12	75 ± 14	-15 ± 1
Sinefungin-MTase	-155 ± 39	-158 ± 15	-104 ± 46	124 ± 30	-16 ± 2

energy of the separated protein and ligand. Table 3 displayed the total MM/PBSA binding energy of panduratin A and sinefungin on the MTase domain, along with the contributions from electrostatics, van der Waals, polar solvation, and non-polar solvation terms. MM/PBSA calculations on the simulated MD trajectory of the MTase-sinefungin complex was with the binding free energy of -155 ± 39 kJ/mol, stronger than the -128 ± 21 kJ/mol of the MTase-sinefungin complex. The significantly lower electrostatic potential term mainly contributed to the stronger binding energy of sinefungin, despite the stronger van der Waals energy of panduratin A. A sinefungin possessed more polar functional groups than a panduratin A, so a higher binding energy penalty for polar solvation slightly weakened the binding of sinefungin.

To assess the local contribution of amino acids and functional groups of ligands to the MM/PBSA binding energy, per-residue decomposition of the energy was performed before the local interaction networks between binding sites and ligands were visualized (Fig. 5). Per-residue binding energy profiles shown in Fig. 5a for both complexes consisting panduratin A and sinefungin, three important binding sites at the regions β2/α4 (His72- Ser77), β3/β4 (Ser101- Asn104), and β6/α6 (Asp133-Asp136) were found with low binding energy. Interestingly, these common binding sites of both complexes were within the S-Adenosyl methionine (SAM) binding pocket and confirmed the capability of both ligands as MTase inhibitors. The difference in total MTase binding energy of a panduratin A and a sinefungin could be further explained from the energy decomposition profiles in Fig. 5a. At the residue Leu103, binding energy contribution within the MTase-panduratin A complex became positive and weakened the protein-ligand binding.

Fig. 5b and c displayed the binding conformations and the interaction networks formed between MTase and the two ligands after 50-ns explicitly solvated MD simulations. Both sinefungin and panduratin A were shown to reside within the SAM binding pocket and near the catalytic tetrad (Lys49, Asp133, Lys173, and Glu206) of SARS-CoV-2 MTase, despite of shifting of binding residues when compared to the molecular docking result. The binding of the ligand at the T-junction consisting of RNA and SAM binding pockets could potentially inhibit the activity by blocking the entrance of RNA substrates to the binding cleft containing the tetrad and the SAM co-substrates to the SAM pocket [29].

Detail of hydrogen bonds, hydrophobic contacts, along with other types of electrostatic and van der Waals interactions formed between binding cleft amino acids and different functional groups of both ligands was found in Table 4, and the nomenclature for functional groups of sinefungin was given in Fig. 6. For the sinefungin-MTase complex, hydrogen bonds were formed between sinefungin and the amino acid residues Gly74, Asp102, and Cys118 at the tail, pyranose, and purine groups. Furthermore, two weak carbon hydrogen bonds and four hydrophobic contacts contributed to the binding. Interestingly, the purine functional group attracted the highest number of interactions at the residues within the α5 region deep into the SAM binding pocket and the β6 region near one of the catalytic tetrad residues at the junction between the RNA pocket and the SAM pocket. For the panduratin A-MTase complex, three hydrogen bonds were formed between the panduratin A and Ala75, Asp102, and Asp104 with the 2,6-dihydroxy-4-methoxyphenyl (Ring III) group. Despite the attractive force from hydrogen bonding, steric clashes at Asp102 still caused stronger repulsion and resulted in the positive local MM/PBSA energy. Besides, three more hydrophobic interactions were found at Leu103, Met134, and Phe152 via Pi-Alkyl, Pi-Sulfur, and Pi-Sigma interactions, respectively. On the other hand, only two hydrophobic contacts were found at the phenyl ring (Ring I) via the Pi-Pi T-shaped and Pi-Alkyl interactions. Table 4 also showed that the simulated complex of MTase-panduratin A complex still preserved the interactions contributed by residues Met134, Tyr135, and Pro137 seen in the molecular docking results.

Despite the weaker binding energy of panduratin A on MTase relative to that of sinefungin, the minimum distance analysis in Fig. 7 showed that positional binding of panduratin A on MTase brought the inhibiting ligand into proximity with the catalytic tetrad. The minimum Asp133-panduratin A and Lys173-panduratin A distances were found to be 0.5 ± 0.25 nm and 0.75 ± 0.25 nm, respectively (Fig. 7a). Meanwhile, 0.3 ± 0.25 nm and 0.7 ± 0.25 nm minimum distances were found for the Asp133-sinefungin and Lys173-sinefungin pairs (Fig. 7b). The relatively closer distance between panduratin A to the catalytic residues, despite weaker binding energy, still suggested that panduratin A could be an interesting candidate for developing an alternative SARS-CoV-2 MTase inhibitor.

To elaborate on the different structural arrangements of panduratin A and sinefungin within the binding pocket of MTase, the chemical characteristics of functional groups could be considered. A sinefungin, known as an MTase inhibitor binding within the SAM pocket, was an adenosine derivative consisting of a purine group and a pyranose group (ribose sugar) and was capped with an amino acid-like tail. The only difference functional group of sinefungin from the SAM co-substrate was replacing the S-methyl (S–CH$_3$) group with a methylamine (CH$_2$–NH$_2$) group. Therefore, the binding of sinefungin within the SAM pocket was already expected with the purine group buried deep within the SAM pocket, far from the T-junction containing catalytic tetrad, and with the pyranose ring forming up to two hydrogen bonds with Asp102 [30]. However, the tail containing a carboxyl and an amino group became unstable during the MD simulation due to their high solubility. This resulted in the high uncertainty found during the minimum distance measurement. A panduratin A, however, contained an aromatic phenyl ring (referred to in this study as Ring I), a methyl cyclohexene ring (Ring II) connecting to a 2-methyl-2-butene group, and a 2,6-dihydroxy-4-methoxyphenyl (Ring III). According to our analysis, Ring III, which contained two hydroxyl groups and a methoxy group, played both the roles of a pyranose ring and a purine within a SAM substrate, despite the lower amount of interactions deep inside the SAM pocket. However, replacing the water-soluble tails of SAM and sinefungin with a more hydrophobic phenyl group in Ring I of panduratin A could stabilize the interaction with Tyr135 near

a SARS-CoV-2 Nsp16

b

c
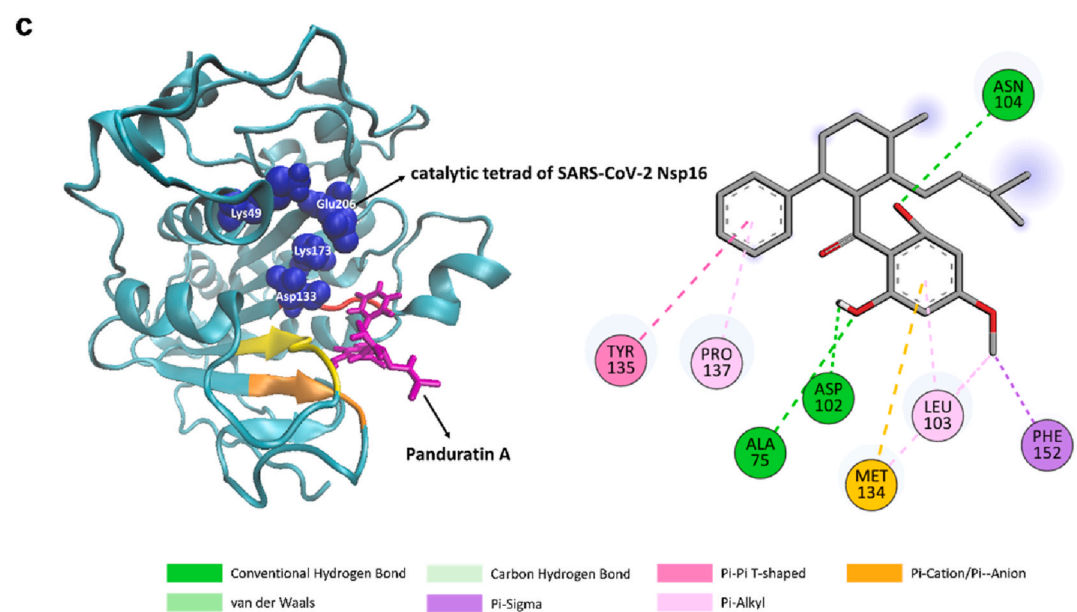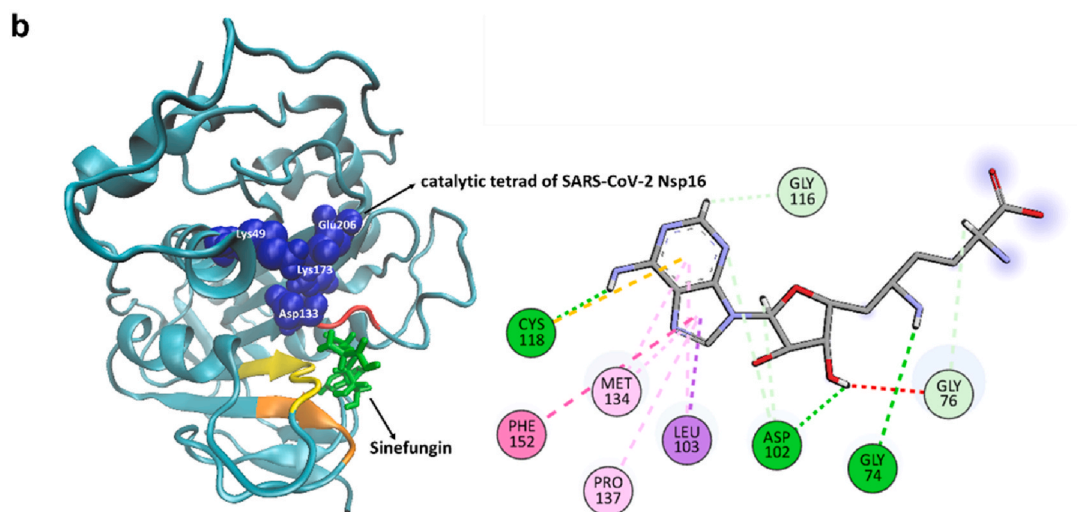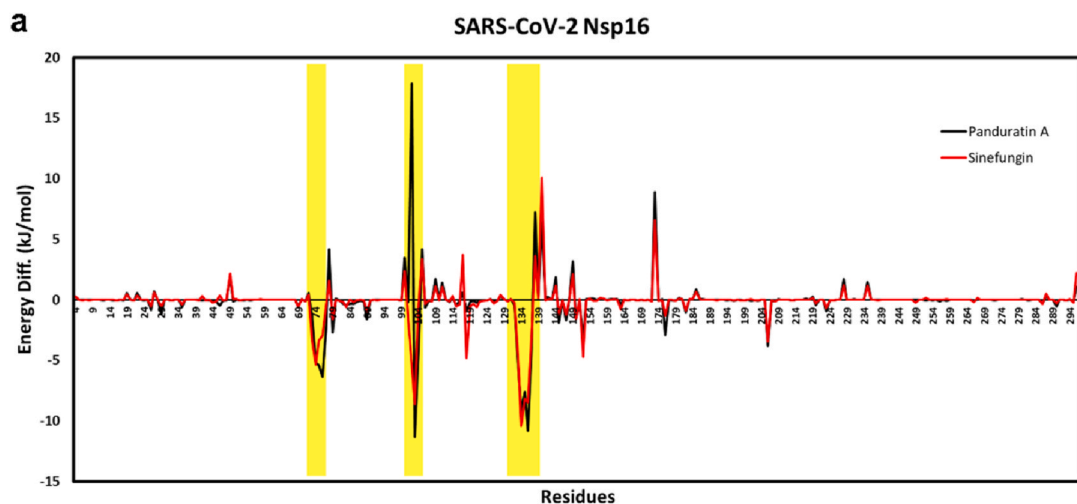
(caption on next page)

Fig. 5. (**a**) The per-residue free energy decomposition of sinefungin (red line) and panduratin A (black line). The 3D and 2D interaction of the docking complex of sinefungin and panduratin A docked into the binding site of the SARS-CoV-2 2′-O-methyltransferase (MTase) (cyan) after MD simulations: (**b**) Sinefungin (green)-MTase complex, (**c**) Panduratin A (pink)-MTasecomplex. The docking imaged were generated using PyMOL Stereo 3D Quad-buffer and Discover studio 2021 was used to map the binding network of a simulation snapshot. (For interpretation of the references to colour in this figure legend, the reader is referred to the Web version of this article.)
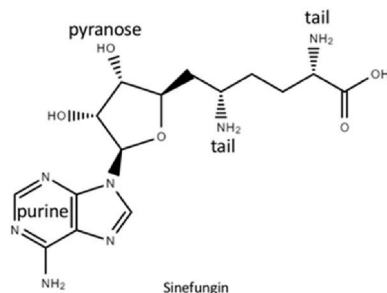

Fig. 6. Schematic representation of a Sinefungin molecule. Functional group labelling as purine, pyranose, and tail were used as references for Tables 2 and 4.

Table 4
Detail of hydrogen bonds, hydrophobic interactions formed between binding cleft amino acids and different functional groups of both ligands.

Region	Residue	Sinefungin			Panduratin A	
		tail	pyranose	purine	Ring I	Ring III
β2	Gly74	🟩				
β2/α4	Ala75					🟩
β2/a4	Gly76	🟩 (light)				
β3	Asp102		🟩			🟩
β3/β4	Leu103		🟪			🟪 (light pink)
β3/β4	Asn104					🟩
β4	Gly116			🟩 (light)		
α5	Cys118			🟩		
β6/α6	Met134			🟪 (light pink)		🟧
β6/α6	Tyr135				🟪 (pink)	
α6	Pro137			🟪 (light pink)	🟪 (light pink)	
α7	Phe152			🟪 (pink)	🟪 (light pink)	🟪

* Conventional hydrogen bond (green), carbon hydrogen bond (light green), Pi-sigma (purple), Pi-Pi T-shaped (pink), Pi-alkyl (light pink), Pi-cation/Pi-anion (orange)
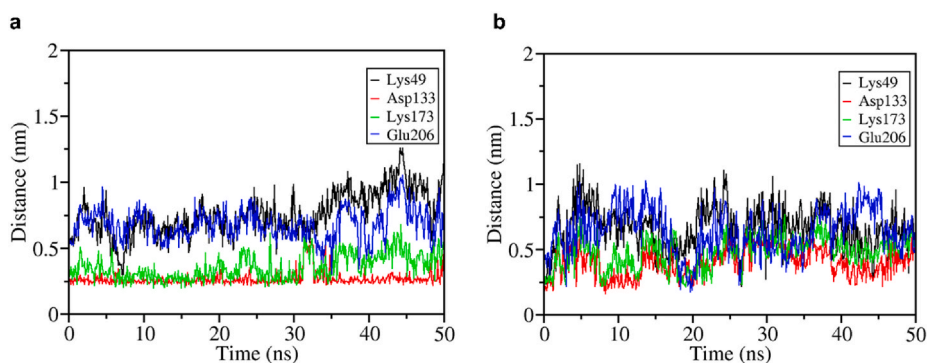

Fig. 7. The minimum distance graph of protein-ligand interactions. The interaction distance between the protein and ligand in MTase protein shows the residues better shielding the catalytic tetrad: (a) MTase-panduratin A and (b) MTase-sinefungin.

the catalytic tetrad, which resulted in a smaller distance from a catalytic residue at Asp133.

4. Conclusions

In conclusion, we proposed that panduratin A has a strong affinity for SARS-CoV-2 Mtase over the other protein targets and could be an interesting alternative to sinefungin. Furthermore, as the inhibition of Mtase could prevent SARS-CoV-2 viral entry, replication, and immune response avoidance, the use of panduratin A along with the cocktail of other bioactive chemicals from herbal extracts that target different pathways could be improved and developed into novel medications or immune boosters for COVID-19 in the future. In addition, the information on the molecular interactions of panduratin A and SARS-CoV-2 target proteins provided by this study could be further proved by further *in vitro* studies to validate the *in silico* results and to monitor the antiviral mechanisms at the cell level.

Author contribution

In conceptualization, PB designed the study. PB and TS analyzed and interpreted the data. Finally, PK, TS and PB critically revised it for important content. All authors have read and agreed to the published version of the manuscript.

Declarations

Declaration of competing interest

The authors declare that they have no known competing financial interests or personal relationships that could have appeared to influence the work reported in this paper.

Acknowledgements

Appendix A. Supplementary data

Supplementary data to this article can be found online at https://doi.org/10.1016/j.heliyon.2022.e12780.

References

[1] D. Cucinotta, M. Vanelli, WHO declares COVID-19 a pandemic, Acta Biomed. 91 (2020) 157–160.
[2] Faheem, et al., Druggable targets of SARS-CoV-2 and treatment opportunities for COVID-19, Bioorg. Chem. 104 (2020), 104269.
[3] Y.A. Helmy, et al., The COVID-19 pandemic: a comprehensive review of taxonomy, genetics, epidemiology, diagnosis, treatment, and control, J. Clin. Med. 9 (2020) 1225.
[4] R. Raj, Analysis of non-structural proteins, NSPs of SARS-CoV-2 as targets for computational drug designing, Biochemistry and Biophysics Reports 25 (2021), 100847.
[5] C.H. Liu, et al., Update on antiviral strategies against COVID-19: unmet needs and prospects, Front. Immunol. 11 (2020), 616595.
[6] S. Belouzard, et al., Mechanisms of coronavirus cell entry mediated by the viral spike protein, Viruses 4 (2012) 1011–1033.
[7] Y. Huang, et al., Structural and functional properties of SARS-CoV-2 spike protein: potential antivirus drug development for COVID-19, Acta Pharmacol. Sin. 41 (2020) 1141–1149.
[8] B. Malone, et al., Structures and functions of coronavirus replication–transcription complexes and their relevance for SARS-CoV-2 drug design, Nat. Rev. Mol. Cell Biol. 23 (2022) 21–39.

[9] E. Decroly, et al., Crystal structure and functional analysis of the SARS-coronavirus RNA cap 2′-O-methyltransferase nsp10/nsp16 complex, PLoS Pathog. 7 (2011), e1002059.

[10] R. Benoni, et al., Substrate specificity of SARS-CoV-2 Nsp10-Nsp16 methyltransferase, Viruses (2021) 13.

[11] M. Bharathi, et al., Silico Screening of Bioactive Compounds of Representative Seaweeds to Inhibit SARS-CoV-2 ACE2-Bound Omicron B.1.1.529 Spike Protein Trimer, Mar Drugs, 2022, p. 20.

[12] R. Kumar, N.A. Murugan, V. Srivastava, Improved binding affinity of omicron's spike protein for the human angiotensin-converting enzyme 2 receptor is the key behind its increased virulence, Int. J. Mol. Sci. 23 (2022) 3409.

[13] C. Chaguza, et al., Rapid emergence of SARS-CoV-2 Omicron variant is associated with an infection advantage over Delta in vaccinated persons, medRxiv 1 (22) (2022), 22269660.

[14] J.T. Ortega, B. Jastrzebska, H.R. Rangel, Omicron SARS-CoV-2 variant spike protein shows an increased affinity to the human ACE2 receptor: an in silico analysis, Pathogens 11 (2021) 45.

[15] Q.A.-N. Fw, et al., In silico study of the potential interactions of 4'-acetamidechalcones with protein targets in SARS-CoV-2, Biochem. Biophys. Res. Commun. 537 (2021) 71–77.

[16] B. Nouadi, et al., Prediction of anti-COVID 19 therapeutic power of medicinal Moroccan plants using molecular docking, Bioinf. Biol. Insights 15 (2021), 11779322211009199-11779322211009199.

[18] Y. Gao, et al., Structure of the RNA-dependent RNA polymerase from COVID-19 virus, Science 368 (2020) 779–782.

[19] A. Khataniar, et al., A comprehensive review of drug repurposing strategies against known drug targets of COVID-19, COVID 2 (2022).

[20] R. Singh, et al., In-silico evaluation of bioactive compounds from tea as potential SARS-CoV-2 nonstructural protein 16 inhibitors, J. Traditional Complementary Med. 12 (2022) 35–43.

[21] P. Kanjanasirirat, et al., High-content screening of Thai medicinal plants reveals Boesenbergia rotunda extract and its component Panduratin A as anti-SARS-CoV-2 agents, Sci. Rep. 10 (2020), 19963.

[22] M. Abbasi, H. Sadeghi-Aliabadi, An in-silico screening strategy to the prediction of new inhibitors of COVID-19 M(pro) protein, Iran. J. Pharm. Res. (IJPR) : IJPR 20 (2021) 125–136.

[23] A. Muhammad, P. Khunrae, T. Sutthibutpong, Effects of oligolignol sizes and binding modes on a GH11 xylanase inhibition revealed by molecular modeling techniques, J. Mol. Model. (2020) 26.

[24] M. Rosas-Lemus, et al., High-resolution structures of the SARS-CoV-2 2'-O-methyltransferase reveal strategies for structure-based inhibitor design, Sci. Signal. 13 (2020).

[25] C.-R. Wu, et al., Structure genomics of SARS-CoV-2 and its Omicron variant: drug design templates for COVID-19, Acta Pharmacol. Sin. 43 (2022) 3021–3033.

[26] K.B. Koziara, et al., Testing and validation of the Automated Topology Builder (ATB) version 2.0: prediction of hydration free enthalpies, J. Comput. Aided Mol. Des. 28 (2014) 221–233.

[27] W. Humphrey, A. Dalke, K. Schulten, VMD: visual molecular dynamics, J. Mol. Graph. 14 (1996) 33–38.

[28] P. Krafcikova, et al., Structural analysis of the SARS-CoV-2 methyltransferase complex involved in RNA cap creation bound to sinefungin, Nat. Commun. 11 (2020) 3717.

[29] M. Wilamowski, et al., 2'-O methylation of RNA cap in SARS-CoV-2 captured by serial crystallography, Proc. Natl. Acad. Sci. U. S. A. (2021) 118.

[30] H. Cohen, et al., Determinants of cofactor binding to DNA methyltransferases: insights from a systematic series of structural variants of S-adenosylhomocysteine, Org. Biomol. Chem. 3 (2005) 152–161.